

**Tunnel magnetoresistance in scandium nitride magnetic tunnel junctions
using first principles**

Authors: Suyogya Karki¹ (suyogya.karki@utexas.edu), Vivian Rogers¹
(vivian.rogers@utexas.edu), Priyamvada Jadaun¹ (priyamvada@utexas.edu), Daniel S.
Marshall²⁻³ (DMarshall@tae.com), and Jean Anne C. Incorvia*¹ (incorvia@austin.utexas.edu)

¹UT Austin Electrical & Computer Engineering Department, 2501 Speedway, EER 3.820, Austin, TX 78712

²TAE Technologies, Inc., 19631 Pauling, Foothill Ranch, CA 92610

³Arizona State University, SEMTE Dept., 501 E. Tyler Mall, ERC 301, Tempe, AZ 85281

* Corresponding author

Abstract

The magnetic tunnel junction is a cornerstone of spintronic devices and circuits, providing the main way to convert between magnetic and electrical information. In state-of-the-art magnetic tunnel junctions, magnesium oxide is used as the tunnel barrier between magnetic electrodes, providing a uniquely large tunnel magnetoresistance at room temperature. However, the wide bandgap and band alignment of magnesium oxide-iron systems increases the resistance-area product and causes challenges of device-to-device variability and tunnel barrier degradation under high current. Here, we study using first principles narrower-bandgap scandium nitride tunneling properties and transport in magnetic tunnel junctions in comparison to magnesium oxide. These simulations demonstrate a high tunnel magnetoresistance in Fe/ScN/Fe MTJs via Δ_1 and Δ_2' symmetry filtering with low wavefunction decay rates, allowing a low resistance-area product. The results show that scandium nitride could be a new tunnel barrier material for magnetic tunnel junction devices to overcome variability and current-injection challenges.

Introduction

Magnetic tunnel junctions (MTJs) are basic building blocks for emerging spintronic devices, including for spin transfer torque magnetic random access memory (STT-MRAM)¹, a leading emerging nonvolatile memory that is steadily transitioning into production, as well as for magnetic logic-in-memory²⁻⁴ and neuromorphic computing^{5,6} applications.

An MTJ consists of a thin insulating tunnel barrier sandwiched between two ferromagnetic (FM) electrodes. When a current is passed across the barrier, parallel (P) magnetization of the two electrodes provides a higher density of states for the majority spin electrons to tunnel across, giving a low resistance, R_P , state. When the magnetization of the two electrodes is antiparallel (AP), the device is in a high resistance, R_{AP} , state. These two states can be used as 1's and 0's for memory and logic applications. The MTJ is characterized by the tunnel magnetoresistance $TMR = \frac{R_{AP}-R_P}{R_P} \times 100\%$ and the resistance-area product $RA = R_P \times A$, where A is the cross-sectional area of the junction.

Progress in MTJ devices has been driven by materials revolutions. Spin-dependent tunneling behavior was first implemented in amorphous aluminum oxide (Al_2O_3) tunnel junctions⁷, which have shown a room temperature TMR up to $\sim 70\%$. About ten years later, a larger TMR was theoretically predicted and then measured in magnesium oxide (MgO) barriers⁸, showing TMR above 600% ⁹ at room temperature in experiments. MgO has been the tunnel barrier of choice for over ten years because of its unique spin transport properties: MgO(001) can lattice match to Fe(001) to prevent mixing of electron states as they tunnel across the barrier, and selectively filters out all tunneling symmetries except the Δ_1 band in Fe. Fe's Δ_1 band is highly spin-polarized and has no available states at the Fermi level in the minority spin, which allows for a theoretically

ultra-high magnetization-dependent tunneling via Bloch waves with small transverse momentum. In the minority spin channel, the smaller conductance is mainly due to interface resonance states¹⁰. However, there are challenges to using MgO that hinder MTJs and their associated technologies from competing with other emerging memories¹¹. A major challenge is that very thin tunnel barriers are necessary. The MgO layer is grown < 1.5 nm thick to have a reasonably low RA product. This is due to both the wide 7.8 eV bandgap of MgO and the metal-insulator band alignment. Pinholes present in this thin layer can create a path for current and degrade the TMR , and when so thin, slight variations of the thickness across a wafer create variations in the TMR and RA product^{12,13}. In addition, an FeO interlayer is created upon annealing at higher temperatures, decreasing expected TMR values in experiment¹⁴. This makes MgO MTJs a challenge to grow, especially compared to competing technologies such as resistive random-access memory. It is also a hindrance for advanced applications of MTJ devices in artificial intelligence and neuromorphic computing, where current may be applied across the tunnel barrier often during real-time adaptation to the environment and where novel switching methods may be used that require higher current across the barrier, causing device breakdown^{15,16}. These challenges lend credence to investigating alternative materials to MgO that can have similar symmetry-filtering transport properties with a narrower bandgap, although no materials have been able to compete with the TMR of MgO to-date at room temperature.

Here, we study using first principles the tunneling properties of scandium nitride (ScN) to understand the material's transport characteristics and determine if MTJs using ScN can achieve high TMR . ScN is chosen for this study because it has a narrower bandgap than MgO (indirect transition from the X to Γ point of 0.9-1.6 eV and direct transition at the X point of 2-2.9 eV¹⁷),

and it has a similar rock salt crystal structure to MgO. ScN(001) is face-centered cubic (FCC) with lattice constant $a = 4.501 \text{ \AA}$ ¹⁷, compared to MgO(001), also FCC with $a = 4.212 \text{ \AA}$ ¹⁸. ScN is a group IIIB transition metal nitride and has not been widely used in device applications¹⁹, but has found niche uses in GaN crystal growth^{20,21} and radio frequency devices²².

There is ongoing research in developing barrier materials with large *TMR* ratios to try to compete with MgO, largely in the class of Mg oxide alloys²³⁻²⁵. In one simulation study, ZnO²⁶ with rock salt structure, bandgap 2.132 eV at the Γ point, and indirect gap of 0.913 eV showed *TMR* = 446% and *RA* = 0.0468 $\Omega\text{-}\mu\text{m}^2$. There is also recent interest in exploring alternate electrode materials for higher spin polarization; one such example is the use of Heusler compounds for both electrodes and barrier materials. Recent work on NiMnSb-MgO junctions²⁷ predicted high *TMR* > 10⁴. To our knowledge, no work has investigated nitride-based tunnel barriers, nor specifically ScN MTJs.

Results

Materials Structure

We investigate the complex band structure of ScN, as well as electron transport in Fe/ScN/Fe MTJs, to understand ScN's properties as a tunnel barrier using density functional theory (DFT) and plane wave conductance techniques. Figure 1a shows the converged ScN lattice with a rock salt crystal structure, and Fig. 1b shows an example converged Fe/ScN/Fe supercell using visualization software VESTA²⁸. Supercells of both Fe/ScN(001)/Fe and Fe/MgO(001)/Fe systems are created for $t = 3-7$ atomic layers of the barrier region to compare the ScN and MgO behavior. In x and y , the unit cell is repeated to infinity; in z the Fe leads extend to infinity in both directions.

To interface with Fe electrodes, the ScN and MgO unit cells are rotated by 45° around the z direction such that the anion atoms (O or N) in the barrier region are positioned directly above the Fe at the interface. After this rotation, the lattice parameter is constrained to the experimental lattice constant of Fe (2.866 \AA) in the x and y directions. This induces a 3.9% in-plane compressive strain in the barrier to match the experimental lattice parameter of MgO (4.212 \AA), and for ScN the experimental lattice parameter of 4.501 \AA is compressed by 11% to match with the leads. These supercells are relaxed using the Vienna ab-initio simulation program (VASP)²⁹⁻³¹ with molecular dynamics. The wavefunctions and resulting conductance of the system are calculated using the Quantum Espresso package³². Magnetization of the Fe electrodes are collinear with the z axis.

The spin up (T^\uparrow) and spin down (T^\downarrow) transmission probabilities, i.e. the probability for transmitting an electron that enters the channel, is calculated. The conductance is then calculated using the Landauer formula $G^\uparrow = \frac{e^2}{h} T^\uparrow$ and $G^\downarrow = \frac{e^2}{h} T^\downarrow$, where e is electron charge and h is Planck's constant for both spin up (majority) and spin down (minority) channels. The Fe electrodes are set up in the P state magnetized in $+z$; for the AP state, the bottom Fe electrode remains in $+z$ and the top is in $-z$. The total conductance (G) for each magnetization state of the electrodes is calculated by adding the conductance from both the spin up and spin down channel, $G = G^\uparrow + G^\downarrow$.

The resulting converged real band structure is shown in Fig. 2 for bulk ScN without and with a Hubbard potential (U) of 4.5 eV added to the 3d orbital of Sc. DFT simulations usually underestimate bandgaps, and the value depends on the pseudopotential used for the calculation. Using the Perdew-Burke-Ernzerhof (PBE) pseudopotential in Fig. 2a, an indirect gap of 0 eV is observed in the band structure. With the additional Hubbard potential, in Fig. 2b there is a direct

gap at the Γ point of 2.99 eV, a direct gap at the X point of 2.28 eV, and an indirect Γ -X gap of 1.31 eV. These results are in agreement with a previous DFT+U simulation, which showed the ScN band structure having a direct gap at the Γ point of 3.39 eV and a direct gap at the X point of 1.55 eV³³. The calculation is also comparable to experimental values, where gaps are observed at the Γ point of 3.8 eV, at the X point of 2.4 eV, and an indirect Γ -X gap of 1.3 ± 0.3 eV³⁴.

Figure 3 shows the complex band structures of ScN (Fig. 3a) and MgO (Fig. 3b) sampled at the Γ and X points. Where the complex band energies intersect with the Fermi energy ($E = 0$) shows the rate of decay of that band in the barrier material. While the band diagram used for conduction calculations agrees with the experimental bandgap, for the complex band calculation of ScN the bandgap is smaller than seen in experiment, which is acceptable for understanding which bands are contributing to conduction (see Supplementary Methods).

For MgO, Fig. 3b shows $\text{Im}(k) = 0.21 \frac{2\pi}{a}$ at the Γ point, showing MgO's Δ_1 band has a low decay rate as expected¹⁰, such that the majority electrons from Fe will continue through the barrier. For ScN, Fig. 3a shows a low decay rate of $\text{Im}(k) = 0.07 \frac{2\pi}{a}$ at the Γ point, as well as a low decay rate of $\text{Im}(k) = 0.07 \frac{2\pi}{a}$ at the X point, showing both Δ_1 and Δ_2' are expected to contribute to tunneling. Since Δ_2' is also spin polarized in Fe (see Supplementary Fig. 1), these results show that ScN junctions are expected to have spin-dependent tunneling, but with contribution from both of these bands, differing from MgO. We also note that even with the narrower bandgap than experiment, we can conclude that the Δ_1 decay rate in ScN is smaller than in MgO, providing higher majority channel conduction than MgO.

Spin-Dependent Transport

In Fig. 4 the transmission probability T for Fe/ScN($t = 6$)/Fe MTJs (top row) is compared to Fe/MgO(6)/Fe MTJs (bottom row) for both spin channels and both magnetic orientations of the Fe electrodes. The plots show the transmission probability for each k_x and k_y point in the supercell Brillouin zone centered at the Γ point, using a 200×200 k -grid. In the transmission plot for the majority P channel of the ScN MTJ, Fig. 4a, we see that conduction occurs at the center of the Brillouin zone (Γ point) and along the X and M points of the tetragonal supercell. The conduction band minimum in the ScN band structure is at the X point and the ScN lattice has been rotated 45° around the z axis for the supercell. As expected, this is reflected in the high transmission lobes around the supercell M points. These peaks corresponding to bulk ScN's X point suggest that the spin-polarized Δ_2' symmetries of the electrodes play a large role in tunneling through ScN junctions, important for optimizing the electrode material for ScN MTJs.

In comparison, the MgO majority P channel, Fig. 4e, shows a broad peak centered at the Γ point via the Fe Δ_1 band. Integrating the majority channel transmission over the Brillouin zone, we find that the total $T_p^\uparrow = 6.44 \times 10^{-3}$ for 6 layers of ScN and $T_p^\uparrow = 1.74 \times 10^{-4}$ for 6 layers of MgO. Figures 4b and 4f show transmission plots of the minority channel for ScN and MgO when the electrode magnetization is parallel. In the minority channel for ScN, $T_p^\downarrow = 8.63 \times 10^{-5}$ and for MgO $T_p^\downarrow = 2.80 \times 10^{-5}$. For the ScN minority P channel we see a peak in transmission at the Γ and X points, whereas the minority P channel of MgO shows transmission around the X points.

Figures 4c-4d show the conduction through ScN when the electrodes have AP magnetization, compared to MgO AP in Figs. 4g-4h. Compared to Figs. 4a-4b, the transmission in the spin up and spin down channels in the ScN system show a much broader peak around the Γ point with lobes

around the X point. In MgO, the transmission peaks for both channels (Fig. 4g and Fig. 4f) are primarily seen around the Γ point, with most transmission around the X point filtered out compared to the *P* minority channel. In the ScN system, the total spin up transmission in *AP* configuration $T_{AP}^{\uparrow} = 2.89 \times 10^{-5}$ and in MgO $T_{AP}^{\uparrow} = 3.25 \times 10^{-7}$. The spin down channels for both ScN and MgO supercells with *AP* magnetization show similar transmission values to that of the spin up channels. The results for Fe/MgO/Fe agree with previous work¹⁰ and give confidence to the validity of the model. As expected, MgO shows high spin filtering: the majority channel dominates conductance compared to the minority channel, and thus parallel magnetized electrodes show a greater than 300 \times increase in conductance compared to antiparallel magnetized electrodes for the 6-layer system. These essential features lead to the high *TMR* seen in MgO MTJs. Promisingly, ScN shows similar spin filtering properties, where, for this layer number, the majority channel in the parallel magnetized electrodes shows a 75 \times higher conductance compared to the minority channel. Also, the conductance is 120 \times higher in the parallel magnetized electrodes compared to the antiparallel electrodes, indicating that ScN MTJs can also achieve high *TMR*.

Magnetic Tunnel Junction Properties

Using the resulting transmission probability values, the conductance ($\frac{e^2}{h}$) for majority and minority channels for *P* and *AP* orientation of the electrodes is shown in Table 1 for ScN and Table 2 for MgO. The total conductance (G) in units of siemens (Ω^{-1}) for each *P* and *AP* configuration is then calculated by summing G^{\uparrow} and G^{\downarrow} . The conductance is converted to *TMR* for the various barrier thicknesses simulated. In our simulations, the $t = 4$ layered system had unstable molecular dynamics convergence and thus was not calculated (see Supplementary Methods). It is seen that in the ScN systems, $TMR = 108\text{-}11,800\%$ showing that ScN can demonstrate large *TMR*. In

comparison, the Fe/MgO/Fe system $TMR = 408-41,800\%$, in agreement with previous simulation results¹⁰. Although simulations predict ultra-high values of TMR for both systems, it is difficult to achieve this in experiments. Our model validates that spin-dependent tunneling is achieved in the ScN MTJs with additional tunneling mechanisms compared to MgO MTJs.

It is observed in Table 1 for Fe/ScN/Fe MTJs there is a non-exponential decay of conductance in each channel with respect to barrier thickness, motivating an explanation for the deviation from the expected relationship seen in MgO MTJs. The breakdown of crystallinity due to lattice mismatch of ScN and Fe electrodes and the unique Δ_2' conduction through the X point could explain this behavior. For the majority channel in MgO, most of the conduction is due to tunneling states with little transverse momentum at the Γ point. In ScN, there are additional tunneling states around the X points, which have electron plane waves of a higher spatial frequency than those around the Γ point. This suggests strong layer-dependent wavefunction interference within the barrier region, as seen in the interface resonance in MgO's minority spin electron transport¹⁰.

In the molecular dynamics simulation, the ScN lattice is compressed in x and y to match the Fe electrodes, buckling the barrier layer slightly and decreasing the crystallinity of the ScN. The simulations show that this atomic convergence varies with respect to barrier layer number. Figures 5a-c show the converged Fe/ScN/Fe structure for $t = 3, 6,$ and 7 atomic layers of ScN. Figure 5d quantifies the deviation $\Delta z_i = z_{Sc} - z_N$ for every barrier layer in each converged MTJ supercell. For the 6 and 8 layer systems, the offset Δz_i is centered at zero, preserving the mirror symmetry in z that contributes to high TMR . This can explain why the TMR is lower in the 3, 5, and 7 layer simulations than the 6 and 8 layer simulations. In a real device, we expect the Fe/ScN interface to

more likely follow the 6 and 8 layer systems' behavior, since the ScN lattice will be allowed to relax.

Figure 6 compares the RA product between ScN and MgO MTJs for varying barrier layer number t . The cross-sectional area of the junction used for the calculation is $8.21 \times 10^{-8} \mu\text{m}^2$. In MgO systems, as t increases, RA increases from 0.203 to $51.0 \Omega\text{-}\mu\text{m}^2$; e.g. for MgO $t = 6$ layers, $RA = 10.5 \Omega\text{-}\mu\text{m}^2$ and $TMR = 30,000\%$. In ScN MTJs, RA ranges between 0.227 and $7.31 \Omega\text{-}\mu\text{m}^2$ and stays low with increasing t ; e.g. for ScN $t = 6$ layers, $RA = 0.326 \Omega\text{-}\mu\text{m}^2$ and $TMR = 11,200\%$. The small decay rate of both Δ_1 and Δ_2' channels, combined with the narrower bandgap of ScN, can explain why the majority channel is highly conductive at all thicknesses simulated.

Calculating the power $W = \frac{I^2 \times RA}{A}$, the power consumed for the $t = 6$ ScN device is 3.11% of that consumed by the MgO device with current held constant. Alternatively, if W is held constant, a 468% increase in the injected current for the ScN MTJ is seen compared to MgO. These results indicate that we expect to see a high TMR in ScN systems with a low RA , enabling either higher current across thin tunnel barriers or thicker tunnel barriers while maintaining the same current, both of which could alleviate the variability and advanced application challenges facing MTJs today.

Discussion

We have shown from first principles that Fe/ScN/Fe MTJs have many of the desirable spin-dependent transport properties of Fe/MgO/Fe junctions, namely a low Δ_1 decay rate through the Γ point, but with additional tunneling pockets through the Δ_2' symmetries at the X point. We have shown this leads to a high TMR , competitive with that in Fe/MgO/Fe. The ScN MTJs also show a

low RA product compared to MgO MTJs, which could be used to overcome variability and current-injection challenges in MgO MTJ devices. These results indicate that ScN could be an exciting new material for MTJ devices, in a field where few alternative materials to MgO have been developed. The work motivates experimental studies, exploration of other lower bandgap materials for advanced MTJ applications, investigation of effects of thermionic emission, and understanding of how the nitrogen-based barrier can affect device properties compared to traditional oxygen-based tunnel barriers.

Methods

VASP

The MTJ supercell was created for various layer numbers (t) for both ScN and MgO systems. The systems with odd t have 6 Fe atoms on the bottom side and 5 Fe atoms on the top side of the supercell. For the $t = 6$ systems, 6 atoms of Fe were placed on each side of the barrier to maintain the periodicity of the system and to ensure a match with the leads in conduction. The supercells were relaxed using the Vienna ab-initio simulation program (VASP) with molecular dynamics such that all forces are < 0.01 eV/Å. The convergence was also done for the total free energy and the band structure energy so that the change between two timesteps is $< 10^{-5}$ eV. Using Perdew-Burke-Ernzerhof (PBE) functionals³⁵, the Fe/ScN/Fe and Fe/MgO/Fe supercells were converged using these cutoffs with an $11 \times 11 \times 11$ k point mesh. The converged supercell atomic positions were then copied into Quantum Espresso to generate wavefunctions of the supercells and perform transport calculations.

Quantum Espresso

To generate the wavefunctions and calculate the complex bands and unit cell conductance, PWscf and PWcond were used from the Quantum Espresso package. The complex bands were generated with a 4-atom tetragonal unit cell for both bulk ScN and MgO using USPP PBE scalar-relativistic pseudopotentials, with the symmetry-resolved real bands sampled in the direction of conduction. Cutoffs of 50 Ry and 500 Ry were used for the wavefunction and charge density cutoffs. For ScN, a Hubbard +U of 8 eV was applied with the ‘pseudo’ projection method, though this was unable to fully correct the bandgap to the values used in the real band structure or MTJ conduction calculations.

After minimizing the energy of the MTJ unit cells in VASP, a PWscf self-consistency field (SCF) calculation was run using Scalar-relativistic PBE functionals with projector augmented wave potentials to generate the wave functions³⁶. For all supercells, 64 Ry and 782 Ry were used for the wavefunction and charge density cutoffs, respectively. Marzari-Vanderbilt smearing³⁷ was used with a broadening parameter of 0.02. For the SCF calculation, an $11 \times 11 \times 1$ Monkhorst-Pack k -grid³⁸ was used. For the systems with parallel magnetization of the leads, both leads were magnetized in the $+z$ direction, with the average magnetization of the Fe atoms converging to roughly $2.3 \mu_B$. For the systems with antiparallel lead magnetization, the atomic positions of the parallel alignment system were duplicated in the $+z$ direction to create an Fe/Barrier/Fe-Fe/Barrier/Fe supercell. The far bottom and top Fe regions were magnetized in $+z$, and the middle Fe region was magnetized in $-z$, where the supercell would be cut in half for conduction calculations. This avoided modeling a discontinuity in magnetization to ensure that the Fe atoms in the barrier supercell matched up to the semi-infinite leads as they would in bulk Fe. The

wavefunctions of the electrode unit cells were generated using the same parameters, except an $11 \times 11 \times 11$ k -grid was used to reflect the cubic nature of the Fe unit cells in the bulk material.

In the SCF stage for the ScN systems, a DFT+U Hubbard offset of 4.5 eV was applied to the Sc atoms via the atomic projection method to match the bandgap with experimental values. We found this value by sweeping the Hubbard offset from 3 to 6 eV for bulk ScN and examining the band structure for each offset. Conductance and k -grid-resolved transmission mapping of each system were calculated with PWCOND under the Landauer-Büttiker³⁹ formalism. With each structure, the barrier supercell (half of the supercell for the antiparallel case) was interfaced to the semi-infinite Fe leads with appropriate magnetization direction. An energy window of 8 Ry was used for reducing the 2D plane wave basis set in transmission for the smaller systems, though the 7-layer systems were reduced to 6 Ry to improve stability. Both were converged to an accuracy of 10^{-8} Ry. The transmission was resolved with a 200×200 k -grid in x and y ; a finely grained k -grid proved important for accurately capturing fine spikes in transmission.

Data Availability

The datasets generated during and/or analyzed during the current study are available from the corresponding author on reasonable request.

Acknowledgements

The authors acknowledge computing resources from the Texas Advanced Computing Center (TACC) at the University of Texas at Austin (<http://www.tacc.utexas.edu>), funding and discussions from Sandia National Laboratories, and funding from the Center for Dynamics and

Control of Materials (CDCM) supported by the National Science Foundation under NSF Award Number DMR-1720595.

Author Contributions

S. Karki and V. Rogers carried out the simulations with assistance from P. Jadaun and prepared the manuscript. D. Marshall provided ideas and discussions of importance to the work. J. A. C. Incorvia led and supervised the work and manuscript.

Competing Interests

The authors declare no competing interests.

References

1. H. Noguchi, K. Ikegami, S. Takaya, E. Arima, K. Kushida, A. Kawasumi, H. Hara, K. Abe, N. Shimomura & J. Ito. 7.2 4Mb STT-MRAM-based cache with memory-access-aware power optimization and write-verify-write/read-modify-write scheme. *2016 IEEE Int. Solid-State Circuits Conf.* 132–133 (2016).
2. D. E. Nikonov & I. A. Young. Benchmarking of Beyond-CMOS Exploratory Devices for Logic Integrated Circuits. *IEEE J. Explor. Solid-State Comput. Devices Circuits* **1**, 3–11 (2015).
3. D. E. Nikonov, G. I. Bourianoff & T. Ghani. Proposal of a spin torque majority gate logic. *IEEE Electron Device Lett.* **32**, 1128–1130 (2011).
4. J. A. Currivan-Incorvia, S. Siddiqui, S. Dutta, E. R. Evarts, J. Zhang, D. Bono, C. A. Ross & M. A. Baldo. Logic circuit prototypes for three-terminal magnetic tunnel junctions with mobile domain walls. *Nat. Commun.* **7**, 3–9 (2016).
5. K. Roy, A. Sengupta & Y. Shim. Perspective: Stochastic magnetic devices for cognitive computing. *J. Appl. Phys.* **123**, (2018).
6. N. Hassan, X. Hu, L. Jiang-Wei, W. H. Brigner, O. G. Akinola, F. Garcia-Sanchez, M. Pasquale, C. H. Bennett, J. A. C. Incorvia & J. S. Friedman. Magnetic domain wall neuron with lateral inhibition. *J. Appl. Phys.* **124**, (2018).
7. J. S. Moodera, L. R. Kinder, T. M. Wong & R. Meservey. Large magnetoresistance at room temperature in ferromagnetic thin film tunnel junctions. *Phys. Rev. Lett.* **74**, 3273–3276 (1995).
8. S. S. P. Parkin, C. Kaiser, A. Panchula, P. M. Rice, B. Hughes, M. Samant & S. H. Yang. Giant tunnelling magnetoresistance at room temperature with MgO (100) tunnel barriers. *Nat. Mater.* **3**, 862–867 (2004).
9. S. Ikeda, J. Hayakawa, Y. Ashizawa, Y. M. Lee, K. Miura, H. Hasegawa, M. Tsunoda, F. Matsukura

- & H. Ohno. Tunnel magnetoresistance of 604% at 300 K by suppression of Ta diffusion in CoFeBMgOCoFeB pseudo-spin-valves annealed at high temperature. *Appl. Phys. Lett.* **93**, 1–4 (2008).
10. W. H. Butler, X. G. Zhang, T. C. Schulthess & J. M. MacLaren. Spin-dependent tunneling conductance of Fe/MgO/Fe sandwiches. *Phys. Rev. B - Condens. Matter Mater. Phys.* **63**, 544161–5441612 (2001).
 11. S. Ikeda, J. Hayakawa, Y. M. Lee, F. Matsukura, Y. Ohno, T. Hanyu & H. Ohno. Magnetic tunnel junctions for spintronic memories and beyond. *IEEE Trans. Electron Devices* **54**, 991–1002 (2007).
 12. L. Xue, A. Kontos, C. Lazik, S. Liang & M. Pakala. Scalability of Magnetic Tunnel Junctions Patterned by a Novel Plasma Ribbon Beam Etching Process on 300 mm Wafers. *IEEE Trans. Magn.* **51**, 1–3 (2015).
 13. J. J. Kan, C. Park, C. Ching, J. Ahn, L. Xue, R. Wang, A. Kontos, S. Liang, M. Bangar, H. Chen, S. Hassan, S. Kim, M. Pakala & S. H. Kang. Systematic validation of 2x nm diameter perpendicular MTJ arrays and MgO barrier for sub-10 nm embedded STT-MRAM with practically unlimited endurance. *Tech. Dig. - Int. Electron Devices Meet. IEDM 27.4.1-27.4.4* (2017).
 14. X. G. Zhang, H. Butler & A. Bandyopadhyay. Effects of the iron-oxide layer in Fe-FeO-MgO-Fe tunneling junctions. *Phys. Rev. B - Condens. Matter Mater. Phys.* **68**, 6–9 (2003).
 15. W. S. Zhao, Y. Zhang, T. Devolder, J. O. Klein, D. Ravelosona, C. Chappert & P. Mazoyer. Failure and reliability analysis of STT-MRAM. *Microelectron. Reliab.* **52**, 1848–1852 (2012).
 16. H. Ahmad, J. Atulasimha & S. Bandyopadhyay. Reversible strain-induced magnetization switching in FeGa nanomagnets: Pathway to a rewritable, non-volatile, non-toggle, extremely low energy straintronic memory. *Sci. Rep.* **5**, 1–7 (2015).
 17. H. A. Al-Brithen, A. R. Smith & D. Gall. Surface and bulk electronic structure of ScN(001) investigated by scanning tunneling microscopy/spectroscopy and optical absorption spectroscopy. *Phys. Rev. B - Condens. Matter Mater. Phys.* **70**, 045303 (2004).
 18. W. Eerenstein, L. Kaley, L. Niesen, T. T. M. Palstra & T. Hibma. Magneto-resistance and superparamagnetism in magnetite films on MgO and MgAl₂O₄. *J. Magn. Magn. Mater.* **258–259**, 73–76 (2003).
 19. Z. Gu, J. H. Edgar, J. Pomeroy, M. Kuball & D. W. Coffey. Crystal growth and properties of scandium nitride. *J. Mater. Sci. Mater. Electron.* **15**, 555–559 (2004).
 20. J. Zhang, X. G. Zhang & X. F. Han. Spinel oxides: Δ 1 spin-filter barrier for a class of magnetic tunnel junctions. *Appl. Phys. Lett.* **100**, 2–6 (2012).
 21. C. Constantin, H. Al-Brithen, M. B. Haider, D. Ingram & A. R. Smith. ScGaN alloy growth by molecular beam epitaxy: Evidence for a metastable layered hexagonal phase. *Phys. Rev. B - Condens. Matter Mater. Phys.* **70**, 1–4 (2004).
 22. M. Moreira, J. Bjurström, I. Katardjev & V. Yantchev. Aluminum scandium nitride thin-film bulk acoustic resonators for wide band applications. *Vacuum* **86**, 23–26 (2011).
 23. Ikhtiar, H. Sukegawa, X. Xu, M. Belmoubarik, H. Lee, S. Kasai & K. Hono. Giant tunnel magnetoresistance in polycrystalline magnetic tunnel junctions with highly textured MgAl₂O₄(001) based barriers. *Appl. Phys. Lett.* **112**, (2018).
 24. Y. Miura, S. Muramoto, K. Abe & M. Shirai. First-principles study of tunneling magnetoresistance

- in Fe/MgAl₂O₄/Fe(001) magnetic tunnel junctions. *Phys. Rev. B - Condens. Matter Mater. Phys.* **86**, 1–6 (2012).
25. H. Sukegawa, Y. Kato, M. Belmoubarik, P. H. Cheng, T. Daibou, N. Shimomura, Y. Kamiguchi, J. Ito, H. Yoda, T. Ohkubo, S. Mitani & K. Hono. MgGa₂O₄ spinel barrier for magnetic tunnel junctions: Coherent tunneling and low barrier height. *Appl. Phys. Lett.* **110**, (2017).
 26. H. Tsukahara & H. Imamura. First-principles prediction of ultralow resistance-area product and high magnetoresistance ratio in magnetic tunnel junction with a rock-salt type ZnO barrier. *Jpn. J. Appl. Phys.* **58**, (2019).
 27. Y. Xie, J. Ma, S. Ganguly & A. W. Ghosh. From materials to systems: a multiscale analysis of nanomagnetic switching. *J. Comput. Electron.* **16**, 1201–1226 (2017).
 28. K. Momma & F. Izumi. VESTA 3 for three-dimensional visualization of crystal, volumetric and morphology data. *J. Appl. Crystallogr.* **44**, 1272–1276 (2011).
 29. G. Kresse & J. Furthmüller. Efficiency of ab-initio total energy calculations for metals and semiconductors using a plane-wave basis set. *Comput. Mater. Sci.* **6**, 15–50 (1996).
 30. G. Kresse & J. Hafner. Ab initio molecular dynamics for open-shell transition metals. *Phys. Rev. B* **48**, 13115–13118 (1993).
 31. G. Kresse & J. Furthmüller. Efficient iterative schemes for ab initio total-energy calculations using a plane-wave basis set. *Phys. Rev. B - Condens. Matter Mater. Phys.* **54**, 11169–11186 (1996).
 32. U. Pwscf. PWscf User's Guide (v.6.5MaX). 1–27
 33. M. S. Abu-Jafar, A. M. Abu-Labdeh & M. El-Hasan. The energy band gap of ScN in the rocksalt phase obtained with LDA/GGA+USIC approximations in FP-LAPW method. *Comput. Mater. Sci.* **50**, 269–273 (2010).
 34. D. Gall, M. Städele, K. Järrendahl, I. Petrov, P. Desjardins, R. T. Haasch, T. Y. Lee & J. E. Greene. Electronic structure of ScN determined using optical spectroscopy, photoemission, and ab initio calculations. *Phys. Rev. B - Condens. Matter Mater. Phys.* **63**, 1251191–1251199 (2001).
 35. G. Kresse & J. Hafner. Norm-conserving and ultrasoft pseudopotentials for first-row and transition elements. *J. Phys. Condens. Matter* **6**, 8245–8257 (1994).
 36. P. E. Blöchl, O. Jepsen & O. K. Andersen. Improved tetrahedron method for Brillouin-zone integrations. *Phys. Rev. B* **49**, 16223–16233 (1994).
 37. N. Marzari, D. Vanderbilt, A. De Vita & M. C. Payne. Thermal contraction and disordering of the Al(110) surface. *Phys. Rev. Lett.* **82**, 3296–3299 (1999).
 38. M. Cococcioni & S. De Gironcoli. Linear response approach to the calculation of the effective interaction parameters in the LDA+U method. *Phys. Rev. B - Condens. Matter Mater. Phys.* **71**, 1–16 (2005).
 39. A. Esmaeili, I. R. Vakhitov, I. V. Yanilkin, A. I. Gumarov, B. M. Khaliulin, B. F. Gabbasov, M. N. Aliyev, R. V. Yusupov & L. R. Tagirov. FMR Studies of Ultra-Thin Epitaxial Pd_{0.92}Fe_{0.08} Film. *Appl. Magn. Reson.* **49**, 175–183 (2018).

Figures

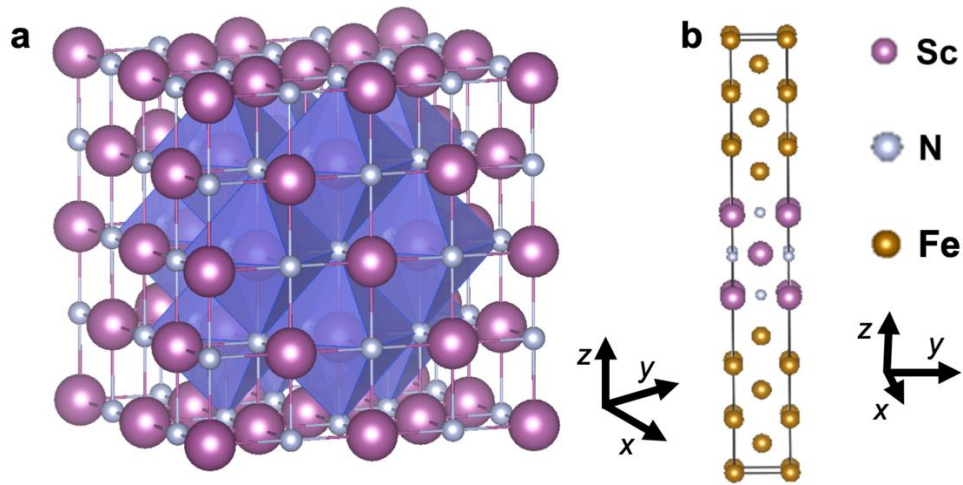


Figure 1. Crystal structure. **a**, Rock salt crystal structure of ScN. **b**, Transport setup of one supercell showing the ScN barrier sandwiched between Fe electrodes with transport along the z direction from the bottom Fe to the top Fe layer. Cells are repeated in x and y to infinity and the Fe electrodes extend to infinity in $+z$ and $-z$.

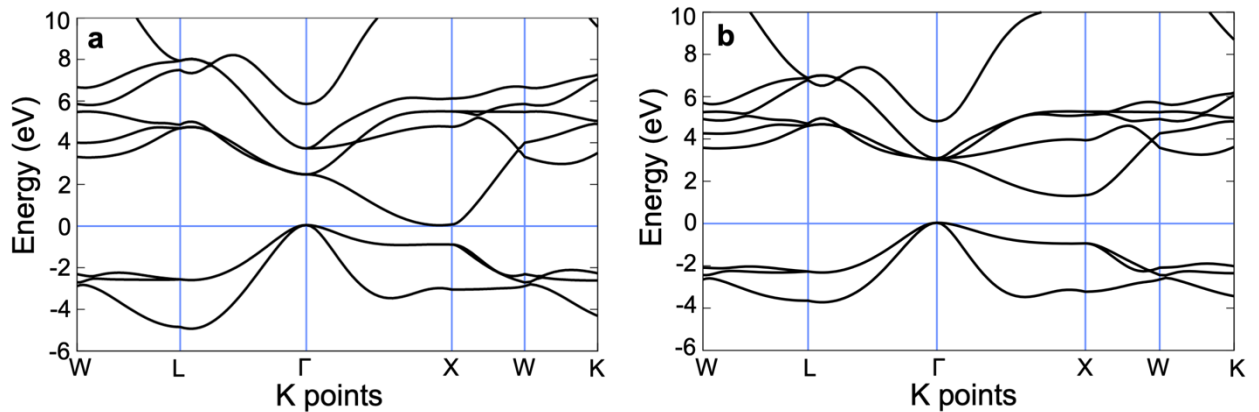


Figure 2. ScN band structure. **a**, Band structure of ScN with direct gap at the Γ point of 2.43 eV. **b**, Band structure of ScN with 4.5 eV Hubbard potential added to the 3d orbital of Sc.

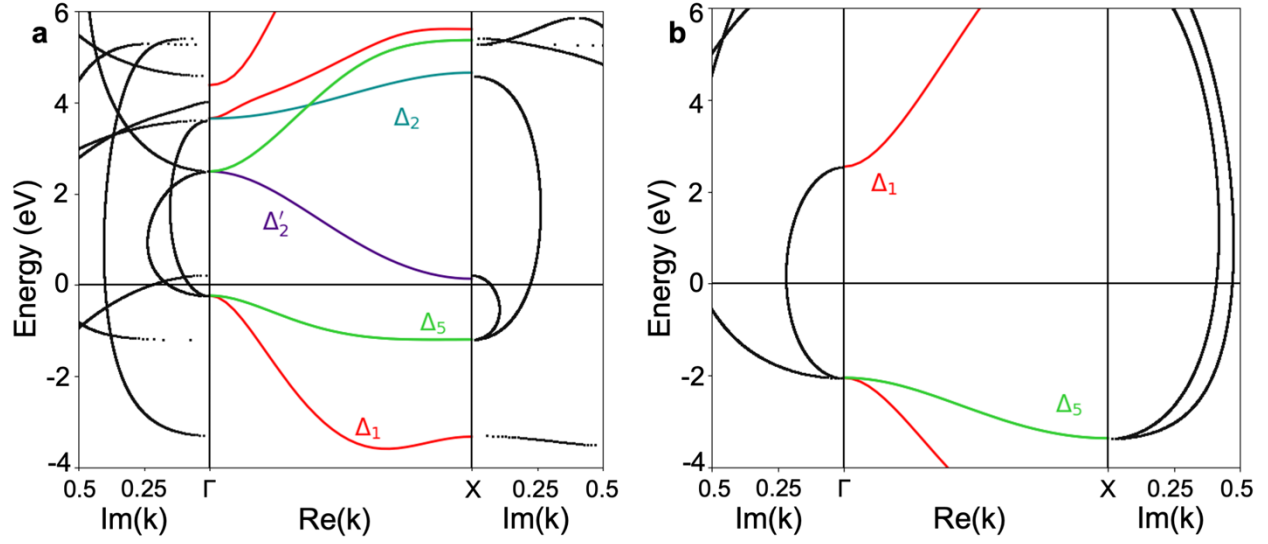


Figure 3. ScN and MgO complex band structure. The complex bands of **a**, ScN and **b**, MgO are shown, sampling into imaginary k space from the Γ and X points with the symmetry-resolved real bands set in-between.

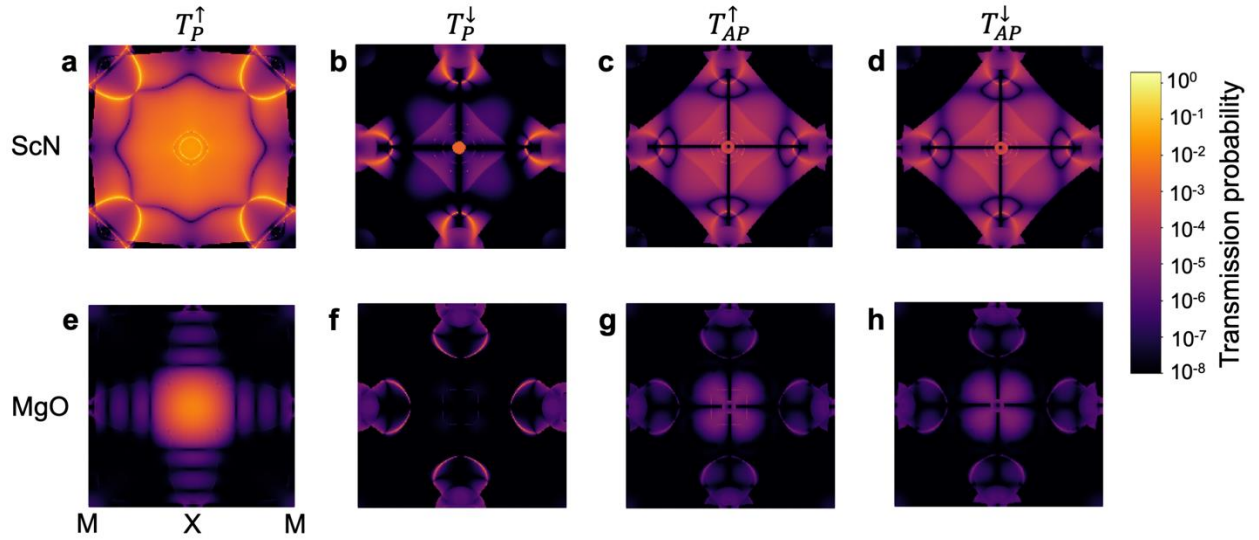


Figure 4. $k_{||}$ -resolved transmission probability. **a-d**, Transmission probability through Fe/ScN($t = 6$)/Fe MTJs, where t is in atomic layers. **e-h**, Transmission probability through Fe/MgO(6)/Fe MTJs. **a,e**, Majority channel for parallel alignment of Fe electrode magnetizations. **b,f**, Minority

channel for parallel alignment of Fe electrode magnetizations. **c,g**, Majority channel (up of input electrode) for antiparallel alignment of Fe electrode magnetizations. **d,h**, Minority channel (down of input electrode) for antiparallel alignment of Fe electrode magnetizations. Color label indicates the transmission probability at each k point. Plots are centered on the Γ point with X and M points labeled in **e**.

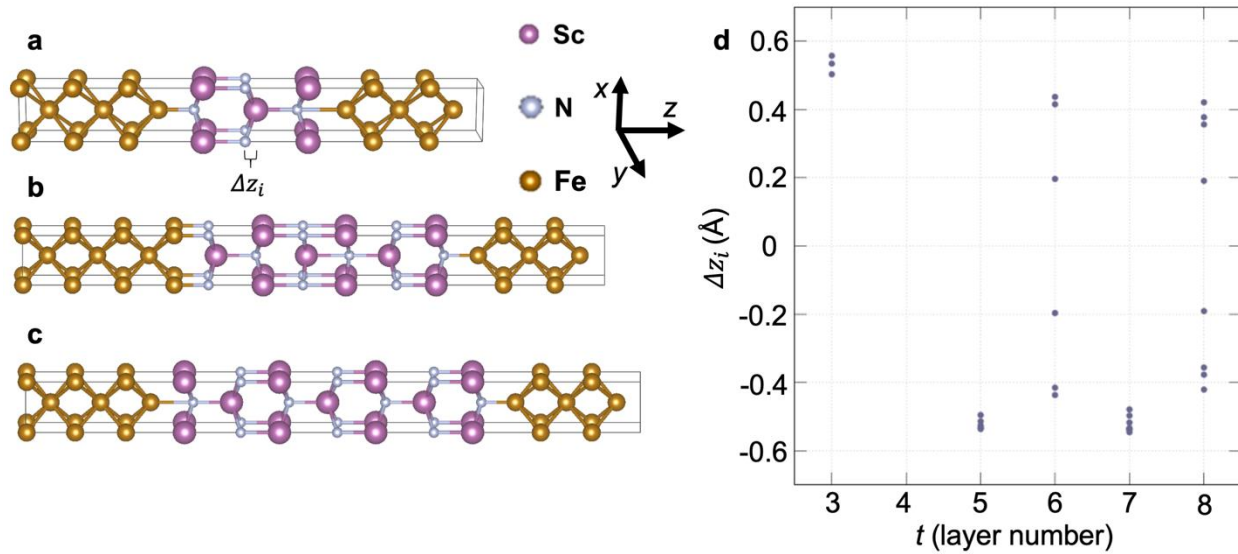


Figure 5. Sc-N displacement. **a**, $t = 3$ layers, **b**, $t = 6$ layers, and **c**, $t = 7$ layers of ScN. Higher *TMR* is observed in the 6 and 8 layer systems where the Sc and N are less displaced from each other in z . **d**, The Sc-N interatomic distance Δz_i plotted for each atomic layer in every converged system.

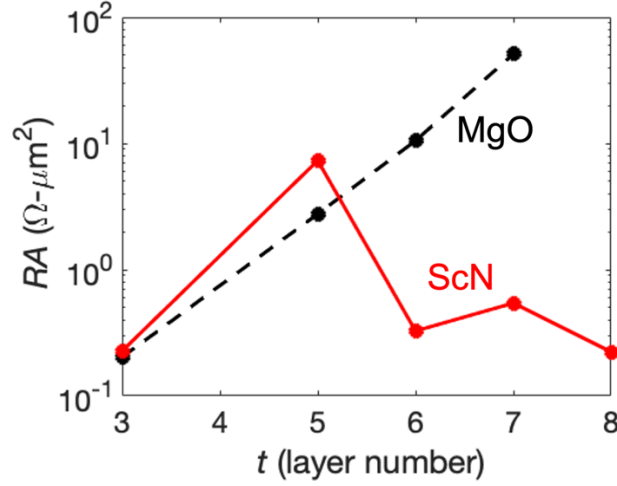


Figure 6. Resistance-area product. Comparison of RA for ScN (red, solid) and MgO (black, dotted) MTJs vs. layer number, showing the ScN MTJ RA stays low while the MgO MTJ RA increases with layer number.

Tables

Layers	G_P^\uparrow (e^2/h)	G_P^\downarrow (e^2/h)	G_P (Ω^{-1})	G_{AP}^\uparrow (e^2/h)	G_{AP}^\downarrow (e^2/h)	G_{AP} (Ω^{-1})	TMR ratio (%)
Fe/ScN(3)/Fe	6.64E-03	2.73E-03	3.62E-07	1.75E-03	1.95E-03	1.47E-07	153
Fe/ScN(5)/Fe	2.09E-04	8.66E-05	1.14E-08	8.01E-05	6.16E-05	5.46E-09	108
Fe/ScN(6)/Fe	6.44E-03	8.63E-05	2.51E-07	2.89E-05	2.59E-05	2.11E-09	11,800
Fe/ScN(7)/Fe	2.96E-03	9.62E-04	1.51E-07	9.63E-05	9.84E-05	7.51E-09	1,920
Fe/ScN(8)/Fe	9.30E-03	2.64E-04	3.69E-07	5.19E-05	8.75E-05	5.39E-09	6,750

Table 1. ScN MTJ conductance and tunnel magnetoresistance. For each barrier layer number studied, conductance values for parallel (G_P) and antiparallel (G_{AP}) alignment in units of (Ω^{-1}) and for majority and minority channels in parallel and antiparallel alignment of the electrodes G_P^\uparrow , G_P^\downarrow , G_{AP}^\uparrow , G_{AP}^\downarrow , respectively, in units of (e^2/h), and corresponding TMR .

Layers	G_P^\uparrow (e^2/h)	G_P^\downarrow (e^2/h)	(Ω^{-1})	G_{AP}^\uparrow (e^2/h)	G_{AP}^\downarrow (e^2/h)		TMR ratio (%)
Fe/MgO(3)/Fe	9.88E-03	5.94E-04	4.04E-07	1.12E-03	6.82E-04	6.96E-08	408
Fe/MgO(5)/Fe	7.55E-04	1.34E-05	2.96E-08	3.88E-06	3.81E-06	2.96E-10	9,700
Fe/MgO(6)/Fe	1.74E-04	2.80E-05	7.80E-09	3.25E-07	2.77E-07	2.33E-11	30,600
Fe/ MgO(7)/Fe	4.04E-05	1.37E-06	1.61E-09	6.29E-08	3.67E-08	3.85E-12	41,800

Table 2. MgO MTJ conductance and tunnel magnetoresistance. For each barrier layer number studied, conductance values for parallel (G_P) and antiparallel (G_{AP}) alignment in units of (Ω^{-1}) and for majority and minority channels in parallel and antiparallel alignment of the electrodes G_P^\uparrow , G_P^\downarrow , G_{AP}^\uparrow , G_{AP}^\downarrow , respectively, in units of (e^2/h), and corresponding TMR .

